High-resolution optical imaging of single magnetic flux quanta with a solid immersion lens

Siddharatha Thakur, Philippe Tamarat, Antonine Rochet, Joschka Birk, Ivan S Veshchunov, Malo Bezard, Alexander I Buzdin, Jean-Baptiste Trebbia, Brahim Lounis

High-resolution optical imaging of single magnetic flux quanta with a solid immersion lens

SIDDHARATHA THAKUR,[1,2] PHILIPPE TAMARAT,[1,2] ANTONINE ROCHET,[1,2] JOSCHKA BIRK,[1,2] IVAN S. VESHCHUNOV,[1,2] MALO BEZARD,[1,2] ALEXANDER I. BUZDIN,[3] JEAN-BAPTISTE TREBBIA,[1,2] AND BRAHIM LOUNIS,[1,2,*]

[1]*Université de Bordeaux, LP2N, Talence F-33405, France*
[2]*Institut d'Optique and CNRS, LP2N, Talence F-33405, France*
[3]*Université de Bordeaux, LOMA, Talence F-33405, France*
**brahim.lounis@u-bordeaux.fr*

Abstract: Magneto-optical imaging of quantized magnetic flux tubes in superconductors – Abrikosov vortices – is based on Faraday rotation of light polarization within a magneto-optical indicator placed on top of the superconductor. Due to severe aberrations induced by the thick indicator substrate, the spatial resolution of vortices is usually well beyond the optical diffraction limit. Using a high refractive index solid immersion lens placed onto the indicator garnet substrate, we demonstrate wide field optical imaging of single flux quanta in a Niobium film with a resolution better than 600 nm and sub-second acquisition periods, paving the way to high-precision and fast vortex manipulation. Vectorial field simulations are also performed to reproduce and optimize the experimental features of vortex images.

1. Introduction

In type II superconductors, an external magnetic field can partially penetrate as filament like flux lines named Abrikosov vortices carrying a single quantum of flux [1]. With a nanometric core surrounded by circulating supercurrents over a distance given by the London penetration depth λ_L (typically λ_L ~100 nm in Niobium), these vortices represent the most compact magnetic objects in superconductors. It has been shown that they have the potential of widespread use as quantized information bits [2] to design high-density digital cryoelectronics (tens of Josephson junctions per μm^2 [3,4]). The local supercurrents produced by a single vortex placed close to a Josephson junction can also induce Josephson phase shifts and thus affect the Josephson transport properties [5-8]. For the development of various schemes in superconducting electronics [6], it is crucial to implement simple and precise vortex imaging and manipulation methods.

Over the past decades, various vortex imaging techniques have been introduced, including pioneering Bitter decoration techniques [9], Lorentz microscopy [10], scanning Hall probe microscopy [11], magnetic force microscopy [12], scanning electron microscopy [13], scanning superconducting quantum interference device (SQUID) microscopy [14]. While scanning tunneling microscopy is capable of resolving a vortex core (~10 nm) [15] and SQUID microscopy provides sensitivity down to the single electron spin level [16], these local probe techniques are heavy to implement in a cryogenic environment. On the other hand, magneto-optical (MO) imaging [17-19] provides far-field optical images with a wide field of view and can be combined with other optical tools recently developed for single vortex manipulation [20] and generation [21]. MO imaging of individual vortices is based on the Faraday rotation of light polarization in a MO indicator placed onto the superconductor, using a beam path configuration with nearly crossed polarizers [22]. The most commonly used MO indicators are ferrite garnets such as Bismuth substituted lutetium iron garnets (Bi:LuIG), that are grown with

a thickness of a few micrometers on a thick (~500 μm thickness) gadolinium-gallium-garnet ($Gd_3Ga_5O_{12}$, GGG) transparent substrate. However, this MO imaging method suffers from poor spatial resolution of the vortices (apparent vortex diameters $\gtrsim$ 1.5 μm [17]). Indeed, the thickness of the GGG substrate introduces severe spherical aberrations that broaden the point-spread function (PSF), i.e. the spatial distribution of a point-source image, well beyond the optical diffraction limit. Another source of degradation of the vortex images is the residual gap between the superconductor layer and the MO indicator pressed on top of it. This gap places the indicator away from the region where the magnetic field stemming from vortices is the most concentrated [18]. To eliminate both problems, it has been proposed to grow a nanometric layer of MO indicator directly on the superconductor. Using a 40 nm-thick EuSe indicator film, apparent vortex diameters as small as 800 nm have been reported [23]. Yet, this technique has limited versatility since EuSe layers are difficult to fabricate and cause strong light absorption. Moreover, they undergo a magnetic ordering phase transition at 4.6 K that restrict their range of use to liquid helium temperatures and thus superconductors with low critical temperatures [24].

The implementation of optical microscopy with a high numerical aperture (NA) remains a crucial step to achieve high-resolution vortex images associated with strong MO signals. It is challenging since the common high-NA microscope objectives have many lenses subjected to mechanical strains and phase changes at cryogenic temperatures. Moreover, such objectives would not compensate for the spherical aberrations introduced by the thick garnet substrate. In this context, implementing a solid immersion lens (SIL) combined with a single, low-NA aspheric lens is a powerful approach. SIL-microscopy allows immersion with a high refractive index adapted to the sample and was originally developed to achieve higher optical resolutions [25]. It has been successfully used to improve the light extraction efficiency of solid-state single photon sources such as individual quantum dots [26-28] or molecules [29,30]. In MO imaging, a SIL-based objective should also eliminate the strong spherical aberrations introduced by the thick garnet substrate. Here, we address the fundamental optical limitations of vortex MO imaging by coupling the indicator on its substrate to a SIL with a high refractive index n ~2 matching that of the GGG substrate. Using the Weierstrass (i.e. super-hemispherical) SIL geometry [31] to focus and collect light from a subwavelength region in close contact with a superconducting Niobium layer, we achieve MO imaging with single-vortex apparent diameters less than 600 nm. We also demonstrate a significant increase in the vortex MO signals and image acquisition rates. The features of the vortex optical images are well reproduced with vectorial electromagnetic-field simulations, which help optimizing the performance of vortex imaging.

2. Experimental setup

The experimental setup used for single vortex MO imaging is depicted in Fig. 1. A 100 nm-thick Niobium film deposited on a sapphire substrate is cooled below its critical temperature T_c = 8.6 K under a weak external magnetic field that penetrates the superconducting film in the form of quantized flux tubes. The MO indicator pressed on top of the Niobium film is a 2.5 μm-thick garnet of composition $Bi_xLu_{3-x}Fe_{5-z}Ga_zO_{12}$ with x ~ 0.9 and z ~ 1.0 [32]. It is grown on a GGG substrate with a thickness h ~500 μm. This sample is illuminated with a white light LED source filtered at the optical wavelength λ = 550 nm with a bandwidth of 15 nm. This wavelength corresponds to a local maximum in the MO indicator's rotational power (Verdet constant $V \sim 0.16°$ mT^{-1} μm^{-1}) together with a garnet transmission factor of 0.43. The SIL used here is a half-ball lens made of S-LAH79 glass with refractive index n = 2.011 at λ = 550 nm, which nearly matches the GGG index n_{GGG} = 1.97 at this wavelength. We operate this SIL combined with the GGG garnet in the Weierstrass geometry, which exploits rigorous stigmatism in the conjugation of two specific points through a spherical refractive surface [33]. The radius r of the SIL is indeed chosen so that the nearest Weierstrass point coincides at best with the MO indicator. The requirement $r = n \times h$ for such geometry is nearly fulfilled with

the choice of r = 1 mm. The residual mismatch between n and n_{GGG} produces negligible spherical aberrations: The Strehl ratio, which corresponds to the ratio of maximal intensities in the PSF and Airy spots, is indeed greater than 0.989. The overall NA of a SIL-based objective operating in the Weierstrass configuration can be as high as n, provided that the aspheric lens has a NA greater than $1/n$. We use here an aspheric lens with focal length 10 mm and NA = 0.49. However, a holder used to press the SIL onto the GGG garnet (See Fig. 1b) reduces the overall NA of this objective to 0.68.

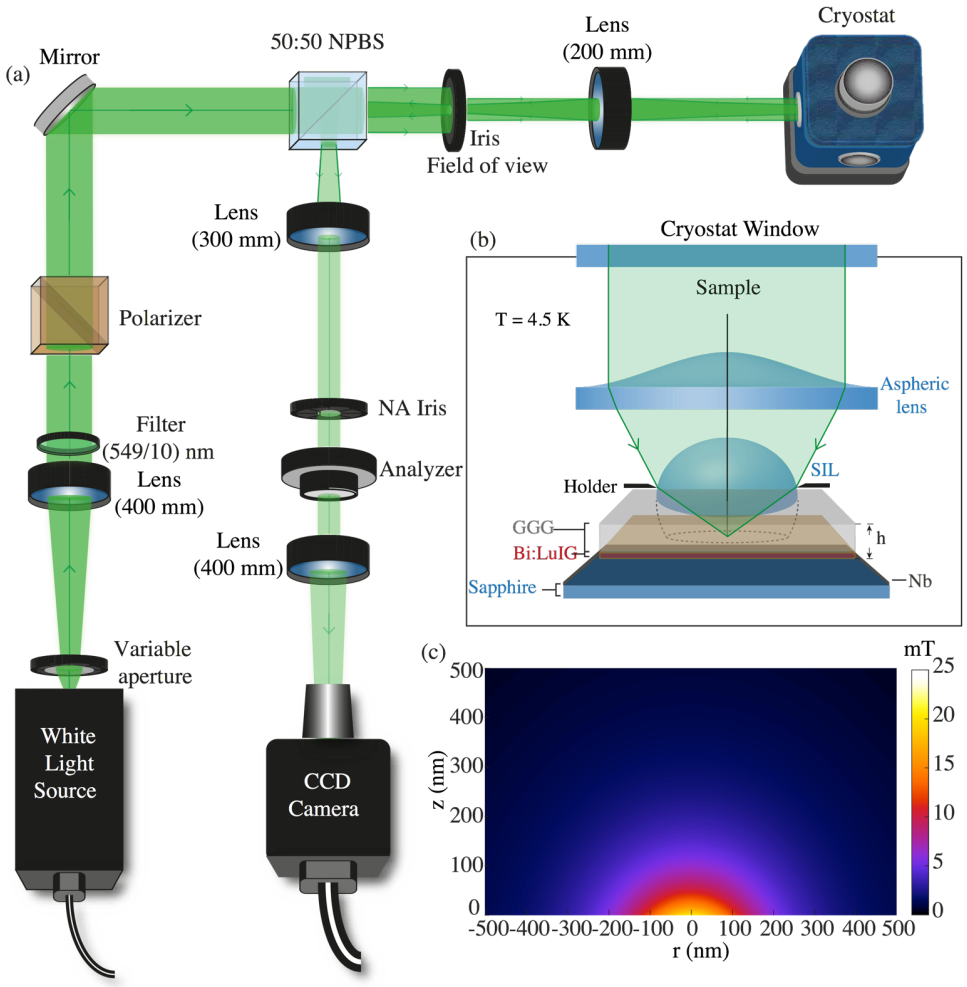

FIG. 1. Optical design for single vortex magneto-optical imaging. (a) The general setup operates on Faraday rotation of light polarization in a Bi:LuIG MO indicator placed on the superconductor in a nearly-crossed-polarizer beam path configuration. (b) The superconductor placed in the cryostat is a Niobium film deposited on a sapphire substrate. The magnetic field stemming from vortices penetrates the indicator and is imaged with a SIL-based objective comprising the SIL and an aspheric lens. The SIL placed on top of the GGG substrate is a half-ball lens operated in the Weierstrass configuration. The white lamp has a fibered output with diameter 3 mm. A source iris controls the aperture of the illumination beam, while a NA iris is placed on the detection path in the Fourier plane of a telescope. A 15 nm bandpass filter is used to collect enough light without introducing significant chromatic aberrations. (c) Simulation of the vertical component of magnetic field $B_z(r,z) = (\phi_0/2\pi)(z-z_0)[r^2+(z-z_0)^2]^{-3/2}$ stemming from a vortex in the half space above the Niobium surface (z =0), r and z being cylindrical coordinates, $z_0 = -1.27\lambda_L$ and λ_L=100 nm [34].

3. Results and discussion

3.1 Vortex images with a solid immersion lens

Figure 2a is a MO image of a spontaneous vortex distribution in a Niobium film at 4 K after field cooling under an external magnetic field of 0.3 Oe, using the aspheric lens alone as in conventional MO imaging setups. A background subtraction scheme is used: An image is acquired above T_c (at 10 K), then subtracted from the image taken at 4 K. The vortices are located at pinning sites that are randomly distributed in the Niobium film. While the real vortex size given by λ_L is ~100 nm in Niobium, the single vortex spots have a full width half maximum (FWHM) diameter of 1.7 µm (Fig. 2a). The addition of the SIL drastically reduces the size of the vortex images by a factor of three (Fig. 2b). As demonstrated in Fig. 2c, a FWHM diameter of 583 nm is achieved. The threefold increase in resolution with the SIL design is evidenced in the case of a higher concentration of vortices: In Fig. 2 d-e, the magnetic field applied during field cooling of the Niobium film is raised to 7.1 Oe, which sets the average inter-vortex distance in the micrometer range. While individual vortices can not be distinguished with a single aspheric lens, they are distinctly resolved with the SIL-based objective.

In order to model the vortex images without and with the SIL, we have computed the vectorial field propagation all along the optical path (z-axis) from the source to the sample and back to the camera with a homemade ray-tracing program [35], taking into account the optical aberrations and changes in polarization at each interface with their Fresnel coefficients. A vortex is considered as a punctual object diffracting light isotropically and producing Faraday rotation of light polarization. Initializing the incident polarization along the x-axis, the PSFs associated to the intensity components I_x and I_y along the x- and y-axes are calculated at the output of the aspheric lens, then projected onto the analyzer axis oriented as in the experiment. The corresponding simulated PSFs are shown in Fig. 2f for the configurations without and with the SIL, keeping the same aspheric lens in both imaging systems. In the case of the aspheric lens used alone (blue curve), the pronounced lobes are due to severe spherical aberrations introduced by the propagation through the GGG substrate. We indeed estimate the peak-to-valley wave-front distortion of ~0.6 λ in this configuration. For a better match with the experimental images, we have added a slight contribution of wavefront distortion 0.03λ caused by deformation of the GGG substrate under non-uniform pressure exerted on its edges to minimize the gap between the Nb film and the MO indicator. This deformation is not taken into account in the SIL configuration, since the flat surface of the SIL exerts a uniform pressure over the central area of the GGG substrate. With the SIL-based objective (red curve), the PSF is nearly diffraction-limited due to the inherent elimination of spherical aberrations.

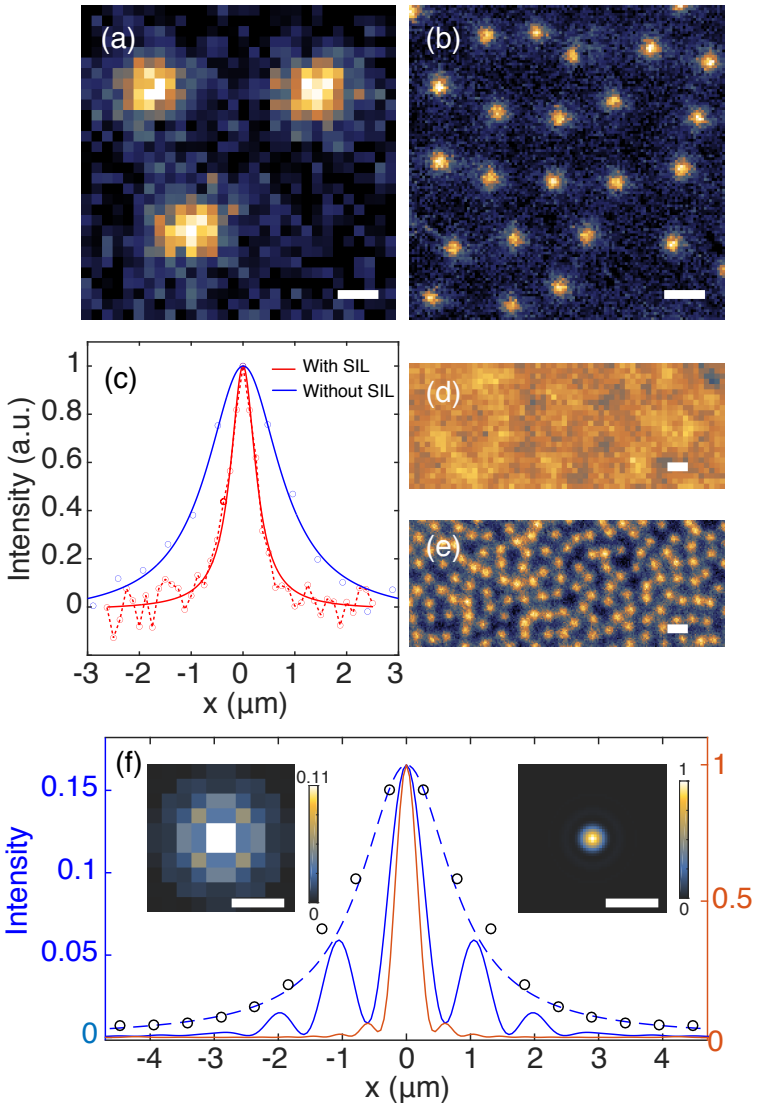

FIG. 2. Optical resolution of vortex images. All scale bars are 2 μm. Single vortices in a Nb film with thickness 100 nm are imaged at 4 K with the aspheric lens alone (a) and with the SIL-based objective (b), under magnetic fields of 0.3 Oe and 2.2 Oe, respectively. The vortices are imaged by a CCD (charge-coupled device) camera (MicroMAX EEVx512FT CCD57, Princeton Instruments) having 512 × 512 pixels with an area of 13 μm × 13 μm. One pixel maps an area of 500 nm × 500 nm in (a). When adding the SIL (b), the magnification of the imaging system is increased by a factor n^2, so that one pixel maps an area 4 × 4 times less. (c) Profiles of the smallest vortex spots imaged without (blue circles) and with (red circles) the SIL, and fitted with Lorentzian curves (blue and red solid curves, respectively). The FWHM diameters are respectively 1.7 μm and 583 nm. Vortices in greater concentration are imaged after field cooling at 7.1 Oe (d) without and (e) with the SIL. (f) Vectorial field simulations of the PSF with the aspheric lens alone (left inset) and with the SIL-based objective (right inset). The blue and red solid curves are the intensity profiles of the respective PSFs calculated from the Debye integral. The black circles represent the cross-section of the left-inset image, taking pixilation into account (pixel size 500 x 500 nm). The dashed blue curve is a Lorentzian profile fitting the circles. Its FWHM of 1.7 μm is in accordance with the experimental vortex spot diameters measured with the aspheric lens used alone.

The evolution of the FWHM vortex spot size, averaged over ~30 vortices, is shown in Fig. 3a as a function of the NA of the SIL-based objective. The NA is varied by controlling the aperture of a diaphragm placed on the detection path in the Fourier plane (See Fig. 1). As expected, the increase in NA leads to sharpening of the vortex spots, whose average size follows the NA-dependence of the diffraction-limited spot diameter $0.61\lambda/\mathrm{NA}$ arising from a point source (solid curve in Fig. 3a). The deviations between the experimental spot sizes and these lower bounds are attributed to residual Nb-BiLuIG gap and to the spreading of the vortex field lines penetrating the MO indicator (see Fig. 1c). At the highest NAs, stronger deviations are observed. They may be due to enhanced optical aberrations, e.g. induced by a slight misalignment of the aspheric lens and SIL optical axes.

3.5 Signal-to-noise ratio

The quality of magneto-optical imaging is also characterized by the signal-to-noise ratio (SNR) of the vortex images. In Fig. 3b, the SNR averaged over ~20 vortices is plotted for both cases, without and with the SIL, as a function of the analyzer offset angle ϕ with respect to the crossed polarizers configuration. Assuming that the noise essentially arises from the photon shot-noise, and that the Faraday rotation angle θ_F of light polarization after the double pass through the indicator is small ($\theta_F \sim 5$ mrad), the SNR can be modeled as

$$\mathrm{SNR} \propto \frac{|\theta_F sin(2\phi)|}{\sqrt{sin^2(\phi)+\epsilon\, cos(2\phi)}} \qquad (1).$$

For both configurations, the experimental data are well reproduced with this expression, using the extinction ratios $\varepsilon = 5 \times 10^{-3}$ and $\varepsilon = 4.4 \times 10^{-2}$ measured without and with the SIL, respectively. On one hand, the higher NA of the SIL-based objective introduces undesired components of light polarization that degrade the extinction ratio. On the other hand, it offers higher photon collection efficiency due to its enhanced NA, which ultimately results in a SNR three times stronger under the same illumination beam, as shown in Fig. 3b.

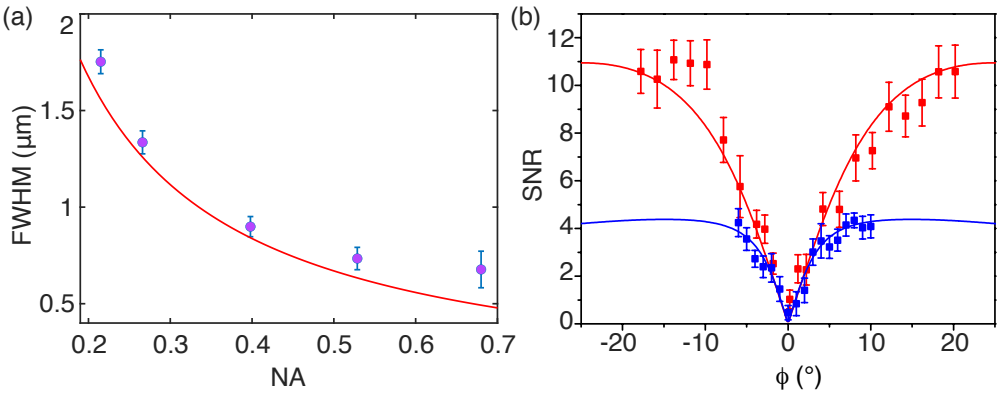

FIG. 3. (a) Average FWHM of vortex images as a function of the effective NA controlled with a diaphragm. The diffraction-limited FWHM is given by the solid curve. (b) The SNR (red squares) of the vortex images is derived as the average ratio of the peak vortex signals to the noise in the background. It is plotted as a function of the analyzer offset angle for the case without (blue) and with the SIL (red) under similar illumination powers. The error bars are indicative of the signal variations amongst vortex spots in the recorded image. The solid curves are plots of Eq. (1), taking $\varepsilon = 4.4\ 10^{-2}$ (red curve) and $\varepsilon = 5\ 10^{-3}$ (blue curve), using the SNR proportionality factor as the only fitting parameter.

An important experimental parameter in vortex MO imaging is the aperture of the light source. While increasing the aperture enhances the illumination intensity in the sample plane, it also promotes depolarization effects that degrade ε and impact the SNR. To model the

aperture dependence of ε, the fibered source with a diameter of 3 mm is modeled by a sum of incoherent, non-polarized and uniformly distributed point sources. Launching 10,000 rays, the three field components are propagated along the optical z-axis towards the sample and reflected towards the analyzer and camera. These fields are then summed incoherently to obtain the intensity components I_x, I_y and I_z as a function of the diameter of the source aperture. The spatial distributions of these three components in the camera plane are displayed as insets in Fig. 4a, in the case of a single source point. As expected, the I_y and I_z components are mainly created when propagating the beam through the aspheric lens and the SIL, and take their greatest values at the largest incidence angles. From these intensity profiles, the extinction ratio $\epsilon = I_y/I_x$ is computed and shown in Fig. 4a as a function of the source diameter. A degradation of ϵ by two orders of magnitude is obtained at the largest diameters. The experimental extinction ratio is displayed in Fig. 4b as a function of the diameter of the source iris. As the source size is reduced below 10 mm down to 2 mm, there is a gain in the quality of extinction by an order of magnitude and a threefold gain in the SNR (Fig. 4c). On the other hand, using large source apertures allows high illumination intensities of the sample and photon flux collection with the SIL, and thus fast vortex imaging. This is illustrated in the series of single-shot images displayed in Figs 4 d-f, recorded for various acquisition times and a fixed aperture of 10 mm. Sub-second imaging with a SNR above unity and a sub-micron resolution is evidenced, which offers great prospects for fast and precise vortex imaging.

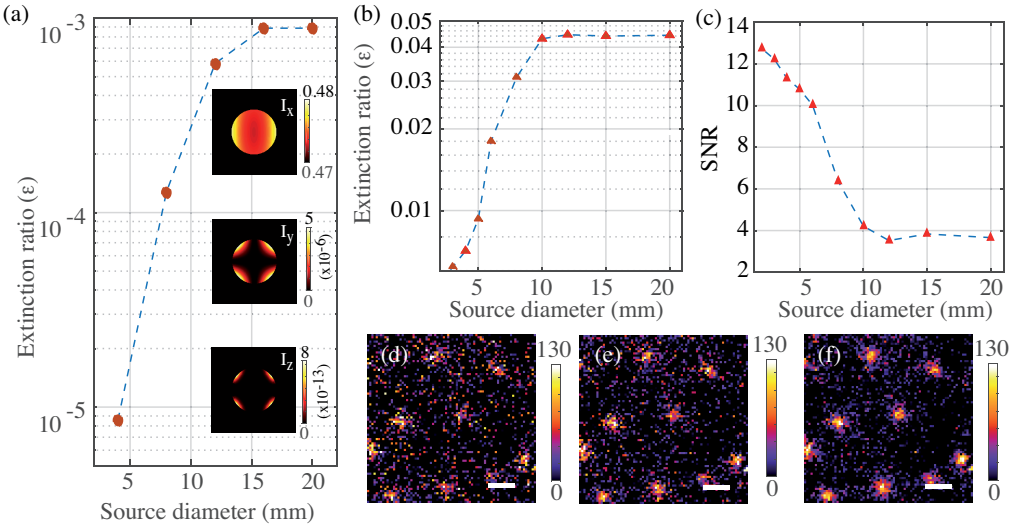

FIG. 4. Influence of the light source aperture. (a) The extinction ratio is computed in the Weierstrass configuration for various diameters of the source beam, using 100 point sources. The insets show the spatial distribution of the intensity components along the x, y and z axes, calculated with a single point source. Experimental evolutions of the extinction ratio (b) and the SNR (c) as a function of the source beam diameter. d-f: Normalized images taken with an integration time of 200 ms (d), 400 ms (e) and 1 s (f), for a source diameter of 10 mm. The SNRs are respectively 0.73, 1.23, 2.45. The scale bars are 2 µm.

4. Conclusion

In conclusion, we have developed a MO imaging setup based on a SIL operating in the Weierstrass configuration and leading to sub-600 nm optical resolution of single Abrikosov vortices. This represents a three-fold improvement in the resolution with respect to single lens imaging systems. Such performance is combined with a higher efficiency in light collection, which is essential for fast acquisition of vortex images. Among the avenues for improvement

of the vortex image quality, higher SNRs could be achieved using a quasi-punctual source for aberration-free illumination of the sample. Greater vortex resolutions and faster vortex imaging could also be reached by increasing the effective NA of the SIL, for instance using a thinner indicator substrate. High-NA MO imaging of vortices with a SIL is thus promising for precise optical localization and manipulation of single vortices applied to the optical operation of Josephson transport [6]. Achieving optical resolutions of the order of the London penetration depth will also enable real-time studies of the forces involved in dense vortex lattices.

Acknowledgments. We acknowledge the financial support from the French National Agency for Research, Région Aquitaine, Idex Bordeaux (Research Program GPR Light), and the EUR Light S&T. B.L. acknowledges the Institut universitaire de France.

Disclosures. The authors declare no conflicts of interest.

Data availability. The data that support the findings of this study are available from the corresponding author upon reasonable request.

References

1. A. A. Abrikosov, "On the Magnetic Properties of Superconductors of the Second Group," Soviet Physics JETP **5**, 1175–1182 (1957).
2. T. Golod, A. Iovan, and V. M. Krasnov, "Single Abrikosov vortices as quantized information bits," Nature Communications **6**, 8628 (2015).
3. S. Tolpygo, V. Bolkhovsky, R. Rastogi, S. Zarr, E. Golden, T. J. Weir, M. L. Johnson, V. K. Semenov, and M. A. Gouker, "A 150-nm Node of an Eight-Nb-layer Fully Planarized Process for Superconductor Electronics," Applied Superconductivity Conference, ASC 2020 Virtual Conference, Vol (15), Issue 49 (Superconductivity News Forum (SNF) **1**, STP669–Wk1EOr3B–01 (2021).
4. I. I. Soloviev, S. V. Bakurskiy, V. I. Ruzhickiy, N. V. Klenov, M. Y. Kupriyanov, A. A. Golubov, O. V. Skryabina, and V. S. Stolyarov, "Miniaturization of Josephson Junctions for Digital Superconducting Circuits," Phys. Rev. Applied **16**, 044060 (2021).
5. T. Golod, A. Rydh, and V. M. Krasnov, "Detection of the Phase Shift from a Single Abrikosov Vortex," Physical Review Letters **104**, 227003 (2010).
6. S. Mironov, E. Goldobin, D. Koelle, R. Kleiner, P. Tamarat, B. Lounis, and A. Buzdin, "Anomalous Josephson effect controlled by an Abrikosov vortex," Physical Review B **96**, 214515 (2017).
7. T. Golod, A. Pagliero, and V. M. Krasnov, "Two mechanisms of Josephson phase shift generation by an Abrikosov vortex," Physical Review B **100**, 174511 (2019).
8. T. Golod, R. A. Hovhannisyan, O. M. Kapran, V. V. Dremov, V. S. Stolyarov, and V. M. Krasnov, "Reconfigurable Josephson Phase Shifter," Nano Letters **21**, 5240–5246 (2021).
9. U. Essmann and H. Träuble, "The direct observation of individual flux lines in type II superconductors," Physics Letters A **24**, 526–527 (1967).
10. K. Harada, T. Matsuda, J. Bonevich, M. Igarashi, S. Kondo, G. Pozzi, U. Kawabe, and A. Tonomura, "Real-time observation of vortex lattices in a superconductor by electron microscopy," Nature **360**, 51–53 (1992).
11. A. M. Chang, H. D. Hallen, H. F. Hess, H. L. Kao, J. Kwo, A. Sudbo, and T. Y. Chang, "Scanning Hall-Probe Microscopy of a Vortex and Field Fluctuations in $La_{1.85}Sr_{0.15}CuO_4$ Films," Europhysics Letters **20**, 645–650 (1992).
12. A. Moser, H. J. Hug, B. Stiefel, and H. J. Güntherodt, "Low temperature magnetic force microscopy on YBa," Journal of Magnetism and Magnetic Materials **190**, 114–123 (1998).
13. D. Koelle, R. Gross, R. Straub, S. Keil, M. Fischer, M. Peschka, R. P. Huebener, and K. Barthel, "Vortex imaging by low-temperature scanning electron microscopy and correlation with low-frequency noise in YBCO DC SQUIDs," Physica C: Superconductivity **332**, 148–155 (2000).
14. B. W. Gardner, J. C. Wynn, D. A. Bonn, R. Liang, W. N. Hardy, J. R. Kirtley, V. G. Kogan, and K. A. Moler, "Manipulation of single vortices in $YBa_2Cu_3O_{6.354}$ with a locally applied magnetic field," Applied Physics Letters **80**, 1010–1012 (2002).
15. D. Roditchev, C. Brun, L. Serrier-Garcia, J. C. Cuevas, V. H. L. Bessa, M. V. Milošević, F. Debontridder, V. Stolyarov, and T. Cren, "Direct observation of Josephson vortex cores," Nature Physics **11**, 332–337 (2015).
16. D. Vasyukov, Y. Anahory, L. Embon, D. Halbertal, J. Cuppens, L. Neeman, A. Finkler, Y. Segev, Y. Myasoedov, M. L. Rappaport, M. E. Huber, and E. Zeldov, "A scanning superconducting quantum interference device with single electron spin sensitivity," Nature Nanotechnology **8**, 639–644 (2013).

17. P. E. Goa, H. Hauglin, A. A. F. Olsen, M. Baziljevich, and T. H. Johansen, "Magneto-optical imaging setup for single vortex observation," Rev. Sci. Instrum. **74**, 141–146 (2003).
18. M. Tokunaga, T. Tamegai, and T. H. Johansen, "Improvement of vortex imaging in magneto-optical technique and Bitter decoration," Physica C: Superconductivity **437-438**, 331–335 (2006).
19. Y. Tsuchiya, Y. Nakajima, and T. Tamegai, "Development of surface magneto-optical imaging method," Physica C: Superconductivity and its applications **470**, 1123–1125 (2010).
20. I. S. Veshchunov, W. Magrini, S. V. Mironov, A. G. Godin, J. B. Trebbia, A. I. Buzdin, P. Tamarat, and B. Lounis, "Optical manipulation of single flux quanta," Nature Communications **7**, 12801 (2016).
21. A. Rochet, V. Vadimov, W. Magrini, S. Thakur, J.-B. Trebbia, A. Melnikov, A. Buzdin, P. Tamarat, and B. Lounis, "On-demand Optical Generation of Single Flux Quanta," Nano Letters **20**, 6488–6493 (2020).
22. P. E. Goa, H. Hauglin, and M. Baziljevich, "Real-time magneto-optical imaging of vortices in superconducting $NbSe_2$," Supercond. Sci. Technol. **14**, 729–731 (2001).
23. D. Golubchik, E. Polturak, G. Koren, and S. G. Lipson, "A high resolution magneto-optical system for imaging of individual magnetic flux quanta," Optics Express **17**, 16160–16165 (2009).
24. J. Schoenes and P. Wachter, "Magnetooptic Spectroscopy of EuS, EuSe and EuTe," IEEE Transactions on Magnetics **12**, 81–85 (1976).
25. S. M. Mansfield and G. S. Kino, "Solid immersion microscope," Applied Physics Letters **57**, 2615 (1990).
26. Q. Wu, R. D. Grober, D. Gammon, and D. S. Katzer, "Imaging Spectroscopy of Two-Dimensional Excitons in a Narrow GaAs/AlGaAs Quantum Well," Physical Review Letters **83**, 2652–2655 (1999).
27. V. Zwiller, H. Blom, P. Jonsson, N. Panev, S. Jeppesen, T. Tsegaye, E. Goobar, M.-E. Pistol, L. Samuelson, and G. Björk, "Single quantum dots emit single photons at a time: Antibunching experiments," Applied Physics Letters **78**, 2476–2478 (2001).
28. W. L. Barnes, G. Björk, J. M. Gérard, P. Jonsson, J. A. E. Wasey, P. T. Worthing, and V. Zwiller, "Solid-state single photon sources: light collection strategies," The European Physical Journal D **18**, 197–210 (2002).
29. J. B. Trebbia, H. Ruf, P. Tamarat, and B. Lounis, "Efficient generation of near infra-red single photons from the zero-phonon line of a single molecule," Optics Express **17**, 23986–23991 (2009).
30. A. Maser, B. Gmeiner, T. Utikal, S. Götzinger, and V. Sandoghdar, "Few-photon coherent nonlinear optics with a single molecule," Nature Photonics **10**, 450–453 (2016).
31. V. Zwiller and G. Björk, "Improved light extraction from emitters in high refractive index materials using solid immersion lenses," Journal of Applied Physics **92**, 660–665 (2002).
32. I. S. Veshchunov, S. V. Mironov, W. Magrini, V. S. Stolyarov, A. N. Rossolenko, V. A. Skidanov, J. B. Trebbia, A. I. Buzdin, P. Tamarat, and B. Lounis, "Direct Evidence of Flexomagnetoelectric Effect Revealed by Single-Molecule Spectroscopy," Physical Review Letters **115**, 027601 (2015).
33. M. Born and E. Wolf, *Principles of Optics: Electromagnetic Theory of Propagation, Interference and Diffraction of Light* (Cambridge University Press, 1999).
34. G. Carneiro and E. H. Brandt, "Vortex lines in films: Fields and interactions," Physical Review B **61**, 6370–6376 (2000).
35. J. B. Trebbia, R. Baby, P. Tamarat, and B. Lounis, "3D optical nanoscopy with excited state saturation at liquid helium temperatures," Optics Express **27**, 23486–23496 (2019).